



IMPROVING OUT-OF-PLANE BEAMFORMING RESOLUTION USING AN ARRAY REDUCTION METHOD

Elias J. G. Arcondoulis¹ and Martinus P.J. Sanders²

¹University of Bristol

University Walk, BS8 1TR, Bristol, U.K.

²University of Twente

Drienerlolaan 5, 7522 NB Enschede, The Netherlands

Abstract

The Adaptive Array Reduction Method (AARM) is an acoustic beamforming array design technique that can generate customised microphone array designs for given problems with given constraints. An array design is achieved through an iterative process of selectively removing microphones from an initial array design. This selection is based on minimizing the impact of removing microphones on the array's point spread function, specifically focusing on preserving an acceptable sidelobe level and main lobe width. In this paper, the AARM is used to enhance the resolution of out-of-plane acoustic beamforming, which is typically known to have lower resolution compared to the in-plane (or planar) resolution. A 48-channel array with aperture of 1 m is specifically designed for each z -distance, for a source located at $(0,0,z_0)$, where in this study $z_0 = 1$ m and $z = 0.5$ m to 3 m. Acoustic beamforming is conducted for each z -plane from which a 3-D source volume is generated, that yields significant out-of-plane resolution than a single array designed for a single z_0 -value with a greater number of microphones.

1 INTRODUCTION

Spiral-based microphone phased array designs provide a well-suited balance between Maximum Sidelobe Level (MSL) and Main Lobe Width (MLW) for varying source locations across a scanning grid and a range of acoustic frequencies [1–3]. One challenge they face, however, is their adaptability for quick customization to specific sound source locations that may deviate from the originally intended sound source location. The Adaptive Array Reduction Method (AARM) [4] is a microphone phased array design method that was developed to enable microphone phased array designs that depart from conventional spiral-based designs [5]. This

method offers a range of customization options and flexibility in designing microphone phased arrays. These arrays can be finely tuned for specific requirements, such as optimizing for a particular beamforming frequency or frequency range, accommodating expected sound source locations situated away from the central axis of the source plane, or adjusting for varying distances between the sound source and the microphone phased array plane. The AARM uses a deterministic iterative microphone removal process, primarily constraining the MSL and MLW criteria to derive an optimized array design from a larger initial array, referred to as the initial stencil.

A challenge that arises from beamforming methods involves accurately determining sound source positions and amplitudes of sources outside the designated source plane, known as out-of-plane resolution. Examples of such problems include identifying noise sources of cars that may arise from varying array-to-source distances [6], and complex situations in industry where the source distance may be unknown [7], to name a few. Conventional acoustic beamforming, using a planar microphone phased array, can be extended into three-dimensional space, by performing beamforming on a series of source planes in the xy -plane while varying their z -coordinates. However, a three-dimensional source map will have low resolution and accuracy in the z -direction [8]. This resolution limitation can be addressed by using two or more planar microphone phased arrays positioned perpendicular to each other at a 90-degree angle [9–12]. However, this method requires additional space and Data Acquisition (DAQ) resources. Therefore, small-scale test facilities, constrained by a limited number of DAQ channels [13], necessitate versatility to fully leverage the potential of their measurement system.

In this paper, the AARM is used to design 48- and 64-channel arrays, each specifically designed for individual source planes within a 3-D volume. Typically, an array is designed for a source located at $(0,0,z_0)$, where z_0 represents the plane for which the array was specifically designed. When the array is used at off-design z -planes, it results in poor out-of-plane resolution. Using the AARM technique, an array can be designed for each z_0 -plane, ensuring that the entire 3-D volume meets the overall design conditions. In this study, $z_0 = 1$ m and z ranges from 0.5 m to 3.0 m. The performance of the optimized arrays in the 3-D grids was compared for the design and off-design conditions.

Performances in 3-D grids, using design conditions and off-design conditions are compared. Experiments were also conducted using a single speaker in an anechoic environment that validated the numerically-predicted out-of-plane resolution.

2 METHODOLOGY

2.1 Conventional Beamforming

A spherical wave source (i.e., a monopole sound source) of unit source strength in stagnant air is simulated. The propagation of a sound wave to the array plane can be represented as \mathbf{p} , a vector of complex pressures (Pa) in the frequency domain, defined as

$$\mathbf{p} = \frac{1}{4\pi |\mathbf{r}_s|} e^{-j2\pi f \mathbf{r}_s / c_0} \quad (1)$$

where f represents both the source frequency and the array design frequency (Hz), c_0 is the speed of sound in air (343 m/s) and m denotes the microphone index number ranging from 1

to M , with M the total number of microphones in the array at each step of the AARM. The vector \mathbf{r}_s links the simulated source location to each of the microphone coordinates in the array plane. The complex pressures at each microphone, as generated in Eq. (1), are used to produce a Cross-Spectral Matrix, C [14] (also referred to as CSM), which is an $M \times M$ matrix defined as

$$C = \mathbf{p}\mathbf{p}^H \quad (2)$$

where H represents the conjugate transpose. The diagonal entries are set to zero, effectively removing the auto-spectra from the matrix [14]. A beamforming output is computed over a planar discretised grid of N data points (scanning grid) at a known distance from the array, typically positioned in line with the centre of the microphone array. Steering vectors, ζ , contain the unique distances of each scanning grid point to each microphone, m . The steering vector formulation for the m^{th} microphone used here [15] is an $N \times 1$ vector defined as

$$\zeta = \frac{1}{4\pi |\mathbf{r}_m|} e^{-j2\pi f \mathbf{r}_m / c_0} \quad (3)$$

where \mathbf{r}_m is the vector between the scanning grid point to the microphone m . The conventional beamforming (CB) output, Y (Pa^2), [15] is computed using

$$Y = \frac{\zeta^H (\mathbf{w}C\mathbf{w}^H) \zeta}{(\sum_{m=1}^M \mathbf{w})^2 - (\sum_{m=1}^M \mathbf{w})} \quad (4)$$

where \mathbf{w} represents an artificial $1 \times M$ microphone shading vector. The shading quantity adjusts the microphone pressures relative to each other. In the AARM technique for producing the array design, the entries of \mathbf{w} (i.e., $w(m)$) are set to either 0 or 1, simulating the removal or inclusion of a microphone in the array, respectively. When an array is initiated, all entries of w are set to 1 to generate the Point Spread Function (PSF).

At each frequency, f , the MLW is calculated first by determining how many scanning grid points the main lobe covers until it decreases by 3 dB from the main lobe peak. This -3 dB definition is consistent with the literature [15–17]. However, the evaluation of the MLW value is unique, based on the square root of the area ratio of the -3 dB main lobe area and the number of scanning grid points, similar to previous array reduction studies [4, 5].

A larger region surrounding the main lobe, called the Main Lobe Area (MLA) is defined here by a threshold of 30 dB below the normalised main lobe peak. Due to the potential asymmetry of the main lobe, the bounds of the MLA are calculated separately in the x - and y -directions, referred to as $\text{MLA}(x)$ and $\text{MLA}(y)$ respectively. The MLA is then excluded from the image source map, ensuring that the remaining source map does not contain any part of the main lobe within 30 dB of its peak. The MSL can then be determined using the maximum remaining Y -value, Y_s . In this paper, the MSL and MLW are represented as follows:

$$\text{MSL (dB)} = 10 \log_{10} \left(\frac{Y_s}{Y_{\max}} \right) \quad (5)$$

$$\text{MLW (\%)} = 100 \times \sqrt{\frac{N_{3\text{dB}}}{N}} \quad (6)$$

where Y_{\max} represents the power of the non-normalised main lobe pressure (Pa^2) and $N_{3\text{dB}}$

denotes the number of scanning grid points occupied by the main lobe from its normalised maximum amplitude (0 dB) down to -3 dB.

2.2 Adaptive Array Reduction Method

The AARM is an advancement of the ARM [5], where the dimensionless metric Φ is defined as the product of the MSL and MLW

$$\Phi = 10 \log_{10} \left\{ \frac{Y_s}{Y_{\max}} \times \frac{N_{3\text{dB}}}{N} \right\} + 20 \quad (7)$$

In the AARM [4], a dimensionless metric, termed $\Phi_{a,l}$, is defined, combining the array's MSL, MLW, and main lobe distortion:

$$\min \{ \Phi_{a,l} \} \equiv \min \left\{ \left[\frac{Y_s}{Y_{\max}} \right]^a \times [N_{3\text{dB}}]^{1-a} \times L_D \right\} \quad (8)$$

where a is a value between 0 and 1, calculated based on previous reduction steps of the AARM, to ensure minimising either the MSL or MLW. The variation of a throughout the simulation is determined by the changes in MSL and MLW as the simulation progresses, specifically their local derivatives with respect to m . These local derivatives are calculated using a five-point-centred finite difference scheme. Details of this procedure and the values of a per iteration can be found in Arcondoulis and Liu [4].

The term L_D is a lobe-distortion metric that measures the size of the MLW in every 45° direction and then takes the ratio of the greatest and smallest values to determine the extent of the distortion in the MLW. For example, a perfectly circular main lobe has $L_D = 1$, indicating no lobe-distortion penalty is applied, while an elliptical main lobe with orthogonal axes of length x and $y = 2x$ will have $L_D = 2$.

In the AARM, an initial array stencil is used, comprising a larger number of microphones, M_i , compared to the desired number of microphones, M_f . Each microphone from $m = 1$ to M_i is shaded one-at-a-time using w . Let m' denote the shaded microphone, such that $w(m') = 0$ and $w(m) = 1$, for $m = 1 : M_i$ where $m \neq m'$. The beamformer output Y is computed for each m' value of m from 1 to M_i . The microphone number m' that yields the minimum $\Phi_{a,l}$ is then removed from the array; removing this microphone minimizes the negative impact on Y . Consequently, array size decreases by one, initiating the next shading process commences: $w(m') = 0$ and $w(m) = 1$, for $m = 1 : M_i - 1$ where $m \neq m'$. This iterative process continues until the desired number of microphones M_f remains within the array stencil.

In this paper, each array is reduced from M_i -channels to M_f -channels and generated at a single design frequency with a source positioned in the centre of the scanning grid ($x = y = 0$) m. The scanning grid used in the AARM simulations comprises $51 \times 51 = N = 2,601$ scanning grid points, covering a $1 \text{ m} \times 1 \text{ m}$ located at various planar distances from the array.

3 NUMERICAL ANALYSIS

3.1 Problem Definition

Utilizing the AARM, we design arrays at a single frequency tailored for various distances between the source plane and array plane, denoted as z_0 , while the plane for acoustic beamforming is denoted as z . Conditions where $z = z_0$ are termed on-design, whereas all other cases ($z \neq z_0$) are termed off-design. The AARM is employed to design arrays across a sweep of z_0 -values from an initial stencil, ensuring the avoidance of off-design scenarios for a range of sound source positions. In this study, both z and z_0 vary from 0.5 m to 3.0 m. For non-AARM arrays, the difference $\Delta z = |z - z_0|$ ranges from 0 to 2.5 m (i.e., 3.0 m – 0.5 m = 2.5 m). Our focus is specifically on 3.5 kHz. However, previous studies have demonstrated that ARM/AARM arrays can deliver performance across a broad frequency range compared to spiral-based arrays with a similar number of microphones [4, 5]. Figure 1 illustrates the distinction between off-design and on-design array design configurations.

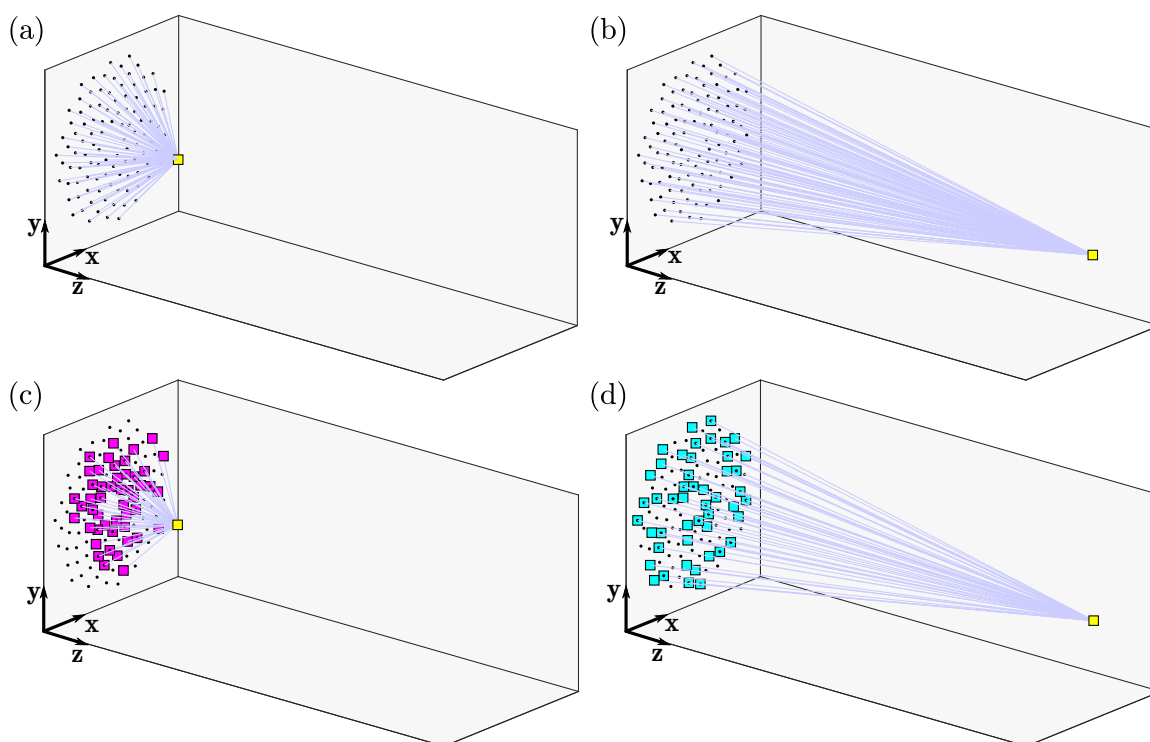


Figure 1: Schematic diagram of acoustic beamforming for two different source positions (z_0 -values), identified by the yellow square. Images (a) and (b) represent a non-AARM array, where the same array is used regardless of source position (i.e., $\Delta z \geq 0$), and (c) and (d) represent unique AARM array designs, reduced from an initial stencil for a specific z_0 -value ($\Delta z = 0$). The light-blue lines represent a set of steering vectors from the source to the array coordinates.

To assess the AARM and its on-design capability across varying z_0 -values, we evaluate two different initial stencil types: a grid-based initial stencil with $M_i = 169$ -channel and a spiral-based initial stencil with $M_i = 105$ -channel (currently used at the University of Twente), as depicted in Fig. 2. The grid array has been used in several numerical and experimental AARM studies [4, 5, 18], while the spiral-based array takes its arrangement from the CAE Systems Bionic M-112 microphone array.

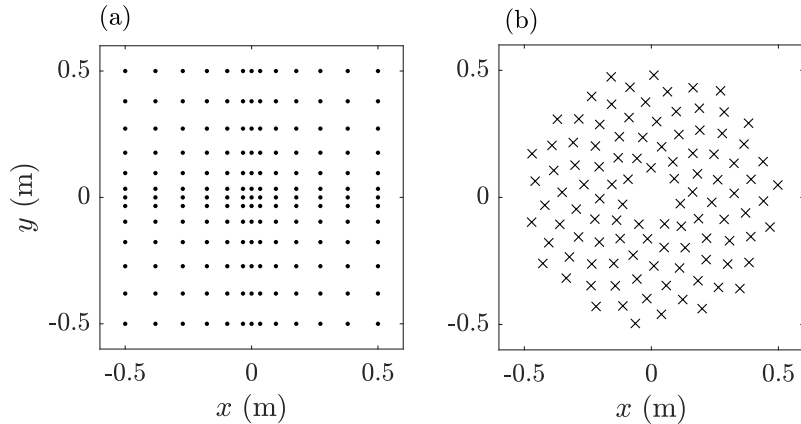


Figure 2: Initial stencils used in this study (a) $M_i = 169$ -channel grid array and (b) $M_i = 105$ -channel spiral-based array.

3.2 Results

Grid-Based Initial Stencils

An illustrative example AARM reduction process is depicted in Fig. 3, using the initial stencil shown in Fig. 2(a). The isosurface in the figure represents the PSF at 3.5 kHz at each stage of the AARM. In other words, a slice of this isosurface for a given microphone number, m , would display the PSF plotted over an xy -source region. At the initial stages of reduction ($m > 130$), grating lobes emerge at 90° to the main lobe due to the equispaced microphones in the initial stencil (typical of grid arrays). The AARM effectively removes the microphones responsible for these grating lobes, particularly those scattered near the boundary and center of the array, evidenced by the comparison between the $M = 169$ and $M = 130$ array patterns. Further reduction from $M = 130$ to $M \approx 65$ demonstrates no notable increase in sidelobe levels (within a -25 dB threshold), albeit a slight expansion in MLW as the array's aperture slightly decreases relative to the initial stencil. However, given the removal of approximately 100 microphones, this compromise is deemed acceptable. Sidelobes only become noticeable for $M \leq 60$ with amplitudes less than -15 dB and scattered about the main lobe.

Figure 4 illustrates 48-channel array patterns designed for a source positioned at $(0,0,z_0)$ and with a scanning grid located at $z = z_0$ (i.e., design point arrays). Generally, arrays designed for smaller z_0 -values tend to concentrate more microphones near the center (owing to the proximity of the source to the array), while the opposite holds true for larger z_0 -design arrays.

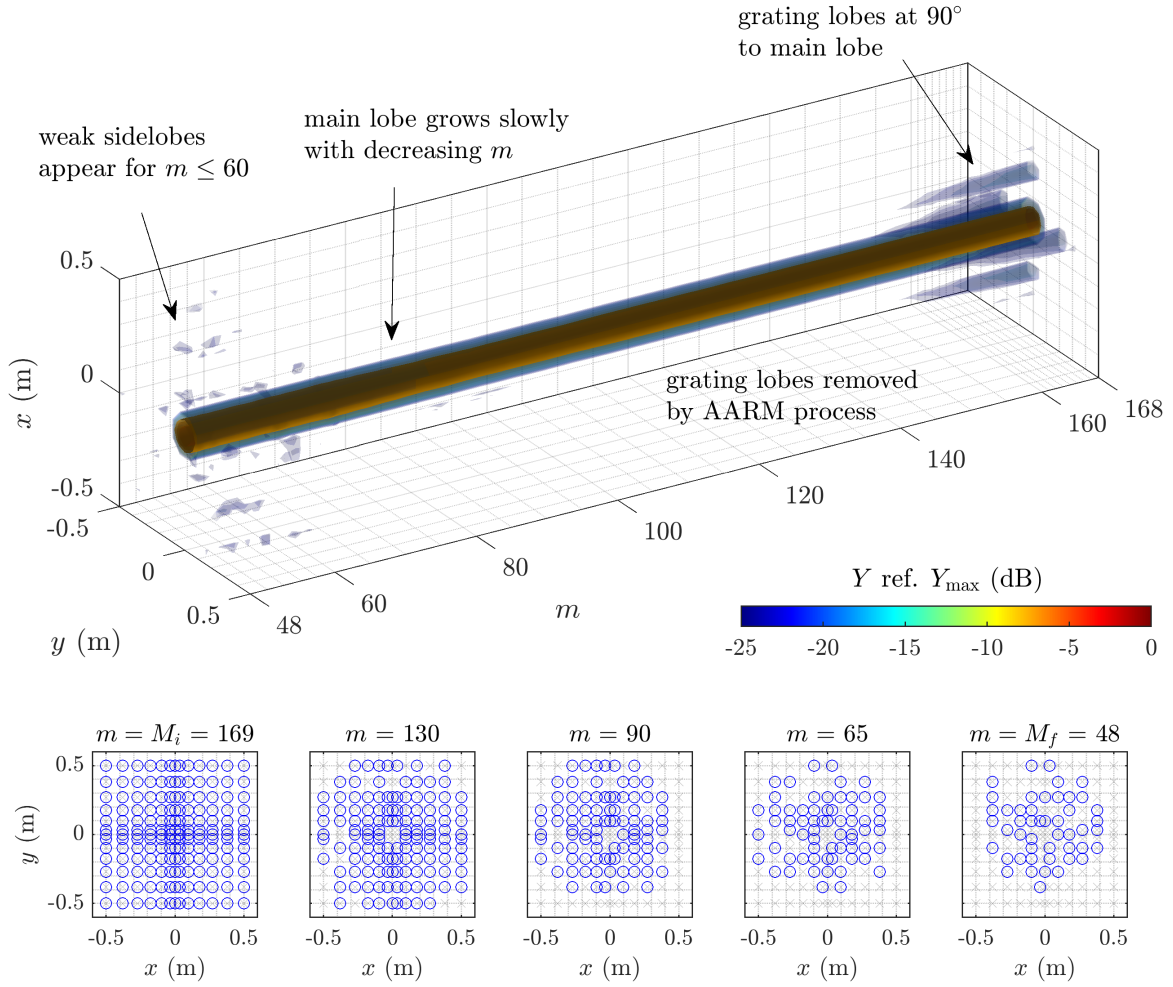


Figure 3: Isosurface of the PSF evolution with the AARM reduction process, from a 169-channel initial stencil (refer Fig. 2(a)) to a final 48-channel array at 3.5 kHz. Some array patterns are also presented that represent stages of the reduction process.

The PSF of the grid-based initial stencil in Fig. 2(a) is presented in Fig. 5 in a 3-D isosurface format. Three slices at 1.5 kHz, 5 kHz and 15 kHz are also presented for clarity. The isosurface represents the PSF over each xy -value. As anticipated for most acoustic arrays, the low frequency PSF is dominated by a large main lobe with no sidelobes, and at much higher frequencies, the main lobe reduces to a small point but the PSF is dominated by sidelobes. Similarly, the PSF of the $z_0 = 1$ m array in Fig. 4 is presented in Fig. 5(b). This isosurface represents the array performance as a function of frequency at the spatial design point (i.e., $z = z_0$) and the vertical axis represents the source frequency, f (Hz). Note that the design frequency of this AARM array is 3.5 kHz and thus all other frequencies within the isosurface are off-design frequencies. Compared to Fig. 5(a), the main lobe at low frequencies is slightly widened due to a reduction in the overall array aperture.

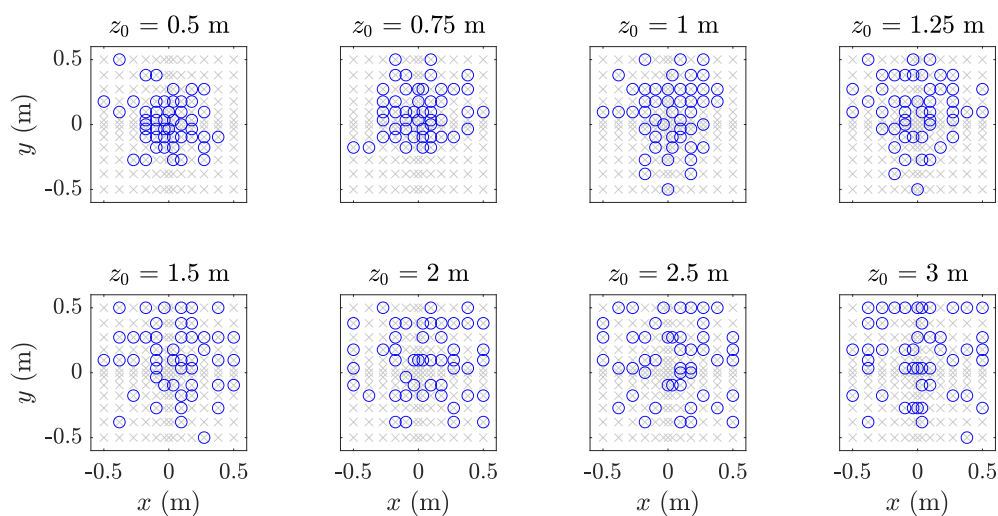


Figure 4: Array patterns using the AARM derived from the grid-based initial stencil in Fig. 2(a), designed for 3.5 kHz. Each array is labeled by their design z_0 -value. The array coordinates are denoted by blue circles and the initial stencil coordinates are denoted by grey crosses.

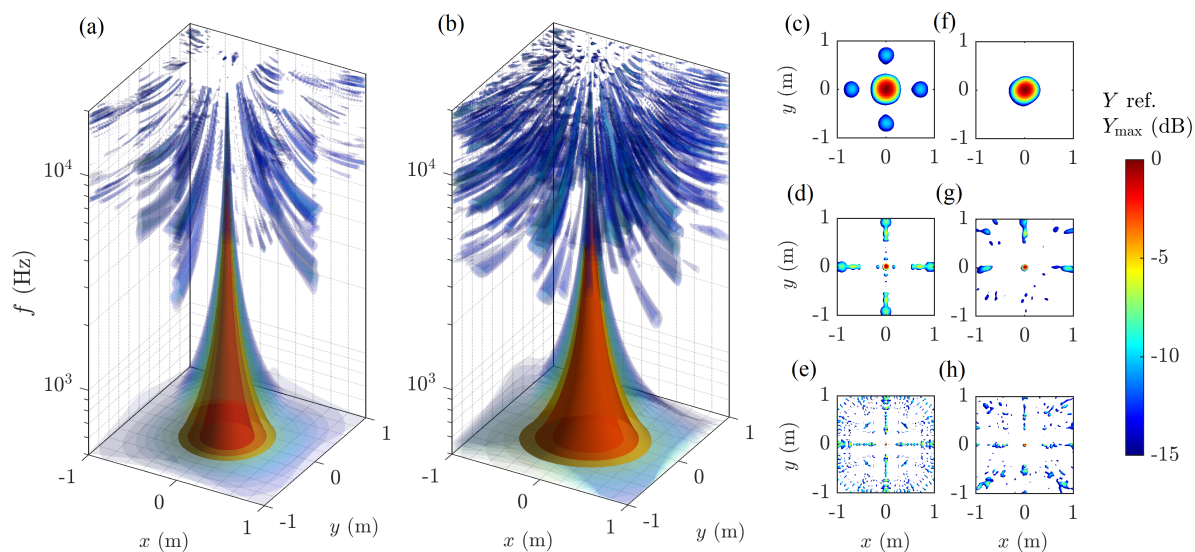


Figure 5: PSF isosurface plots of a source located at $(0,0,z_0 = 1)$ m using the (a) Initial stencil (Fig. 2(a)) and (b) $z_0 = 1$ m array in Fig. 4. Corresponding slices of the initial stencil PSF are presented at (c) 1.5 kHz, (d) 5 kHz and (e) 15 kHz, and of the $z_0 = 1$ m array at (f) 1.5 kHz, (g) 5 kHz and (h) 15 kHz.

Using the on-design arrays enables clear detection of out-of-plane sources (with finite volume), in contrast to an off-design array. This distinction is exemplified in Fig. 6. The off-design array in Fig. 6(a) exhibits the identification of fictitious sources at increasing distances from the true source plane $z_0 = 1.0$ m, each with a broader main lobe than the true source. This phenomenon, well-documented in literature, poses challenges for out-of-plane acoustic beamforming. In contrast, the design-point array configuration in Fig. 6(b) demonstrates a finite main lobe volume with reasonable out-of-plane resolution.

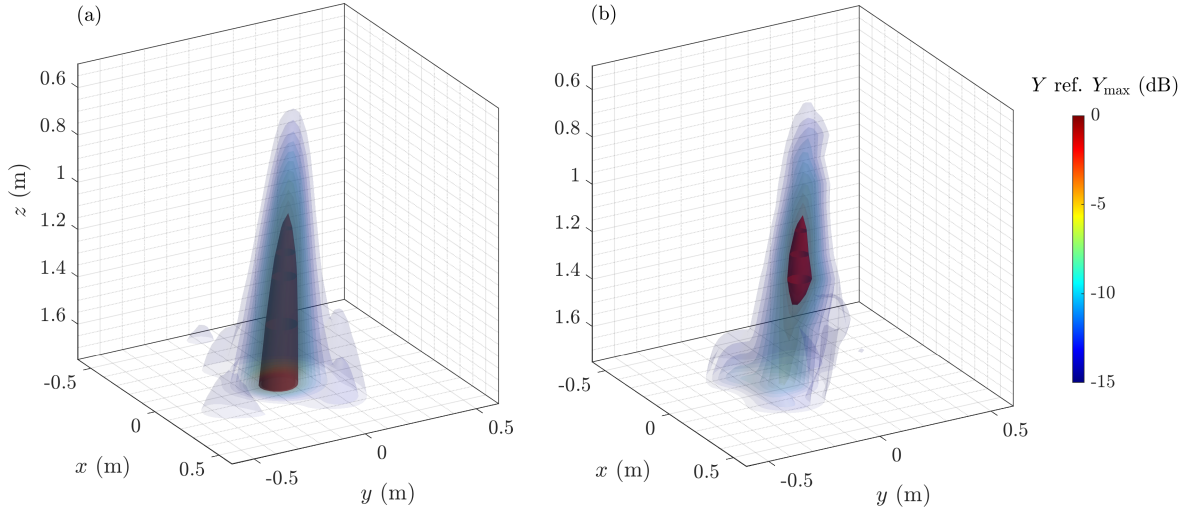


Figure 6: Isosurface plot of a source located at $z_0 = 1$ m and source location attempts using scanning grids from $z = 0.5$ m to 1.75 m. The PSF frequency is 3.5 kHz. (a) off-design array condition and (b) with $z = z_0$ -array design per z -plane.

Spiral-Based Initial Stencils

The AARM, when applied to a grid-based initial stencil, effectively removes grating lobes in the initial stages of the reduction process, as demonstrated in Fig. 3. To mitigate any influence of these 90° grating lobes on the reduction process and final array designs, the spiral-based initial stencil (refer to Fig. 2(b)) is used for the AARM process, as depicted in Fig. 7. A weak ring-shaped grating lobe is initially observed around the main lobe, which diminished during the AARM process and eventually fades (-25 dB below the main lobe peak). Similar to the reduction of the grid-based initial stencil, weak scattered sidelobes emerge in the later stages of the reduction. Array patterns depict an even removal of inner and outer microphones of the array, with no discernible positional bias or microphones clusters.

Array patterns resulting from the AARM using the spiral-based initial stencil and sources located at varying z_0 -values are depicted in Fig. 8. Analogous to the grid-based array designs in Fig. 4, microphones are concentrated near the center for $z_0 < 1.0$ m, while arrays designed with higher values of z_0 tend to distribute more microphones towards the outer regions of the initial stencil. The use of two different stencils (grid-based and spiral-based) provides evidence that the AARM can generate arrays with similar spatial characteristics regardless of the micro-

phone spacing within the initial stencil, presence of microphones in the corners of the available aperture, and number of microphones within the initial stencil.

The PSFs of the spiral-based arrays are depicted in Fig. 9. Similar to the grid-based PSFs shown in Fig. 5, a comparable change in PSF from the initial stencil to the AARM array is observed. The main lobe of the spiral-based initial stencil exhibits minimal asymmetry, and typically, the reduction process results in a slight increase in sidelobe levels by approximately 5-8 dB. These results aim to demonstrate that the AARM, when applied to a spiral-based stencil, performs similarly to its application on a grid-based stencil.

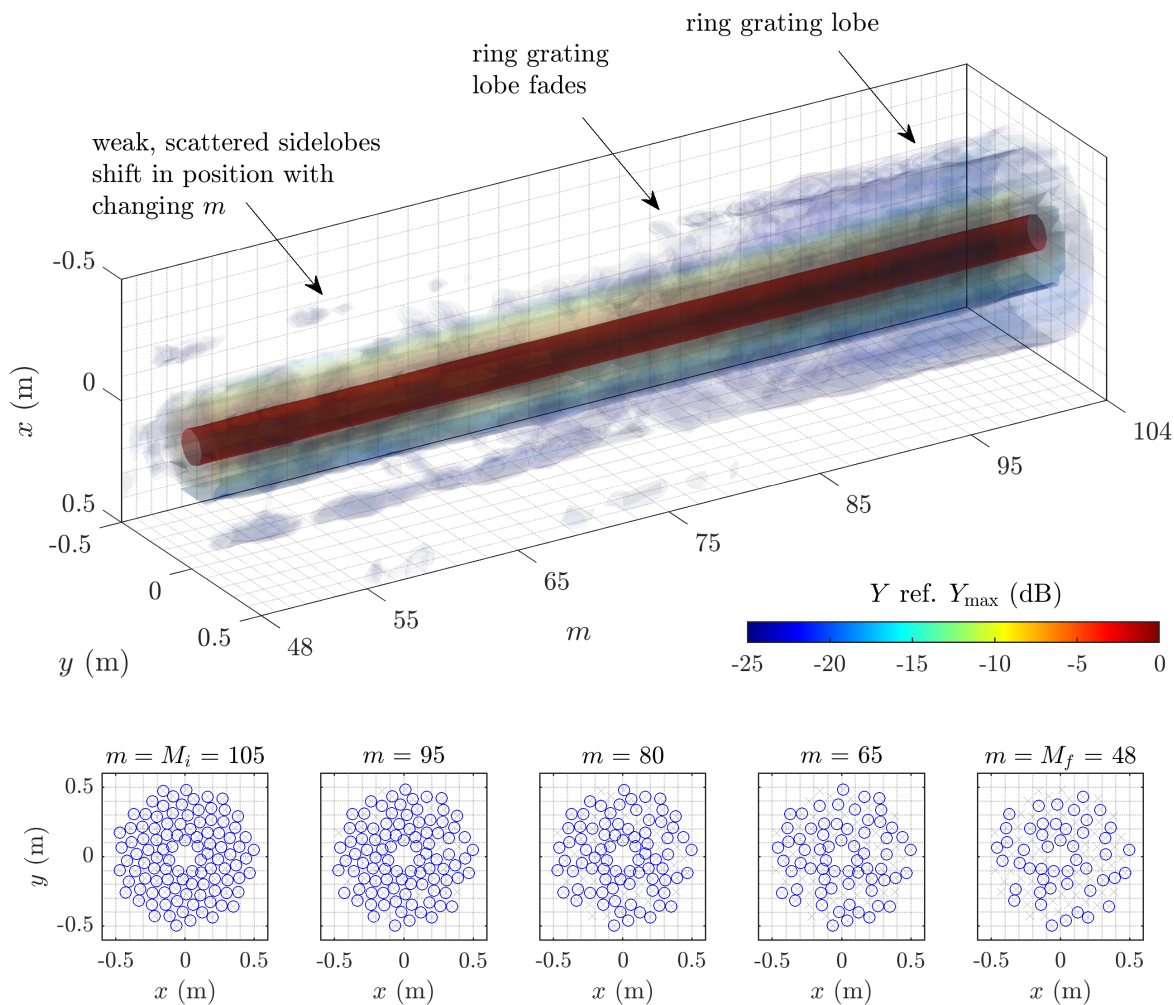


Figure 7: Isosurface plot of the PSF evolution with the AARM reduction process, from a 105-channel initial stencil (refer Fig. 2(b)) to a final 48-channel array at 3.5 kHz. Some array patterns are also presented that represent stages of the reduction process.

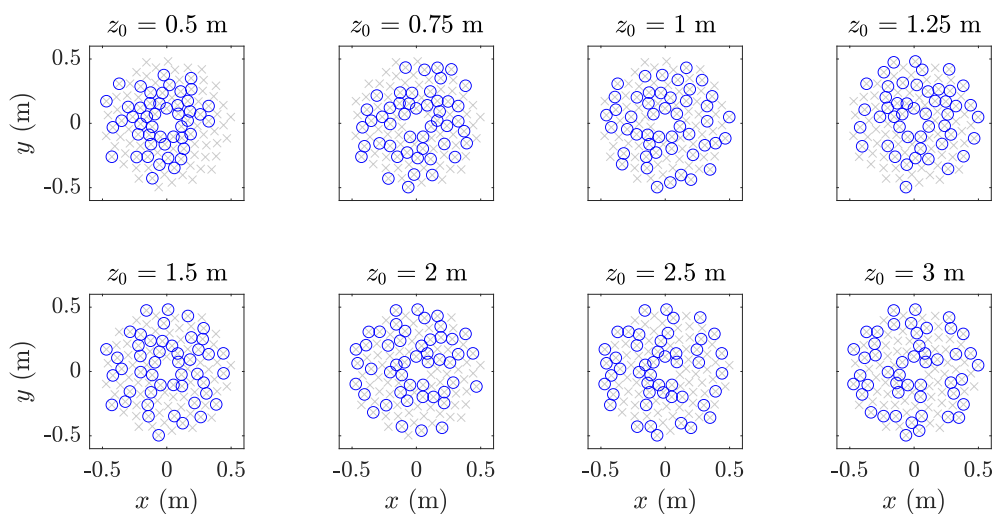


Figure 8: Array patterns using the AARM derived from the spiral-based initial stencil in Fig. 2(b), designed for 3.5 kHz. Each array is labeled by their design z_0 -value. The array coordinates are denoted by blue circles and the initial stencil coordinates are denoted by grey crosses.

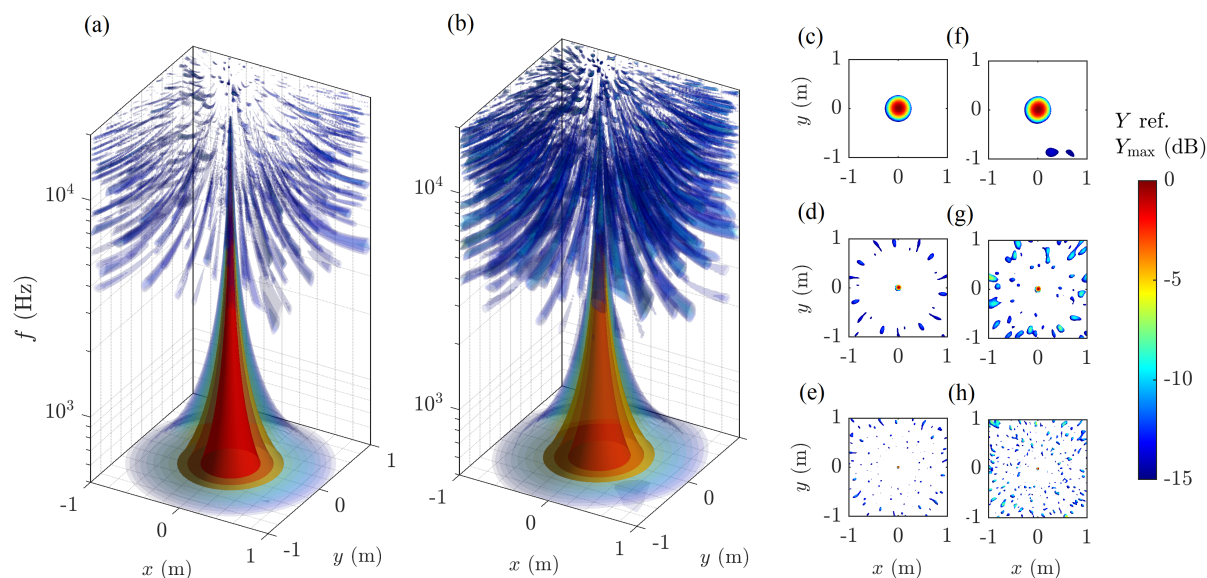


Figure 9: PSF isosurface plots of a source located at $(0,0,z_0 = 1)$ m using the (a) Initial stencil (Fig. 2(b)) and (b) $z_0 = 1$ m array in Fig. 8. Corresponding slices of the initial stencil PSF are presented at (c) 1.5 kHz, (d) 5 kHz and (e) 15 kHz, and of the $z_0 = 1$ m array at (f) 1.5 kHz, (g) 5 kHz and (h) 15 kHz.

In Fig. 10, the PSFs of three distinct z_0 -arrays are presented, with the source positioned at $(x, y, z) = (0, 0, 1.0)$ m. To facilitate comparison, two off-design arrays were used, designed for $z_0 = 0.5$ m and 2.0 m, depicted in Fig. 10(a) and 10(c), respectively. The PSF of the on-design array $z_0 = 1.0$ m is illustrated in Fig. 10(b). Comparison of these three PSF isosurfaces reveals that on-design performance at 3.5 kHz is improved in terms of main lobe width and sidelobe level. The $z_0 = 0.5$ m array demonstrates poorer performance at lower frequencies due to the microphone clustering around the array center, while the opposite holds true for the $z_0 = 2.0$ m array, where microphones are distributed near the outer aperture of the array. Although these results are presented for a single frequency design array and only three z_0 -values, they indicate, to some extent, the effectiveness of the AARM to developing arrays tailored for specific out-of-plane conditions. The subsequent stage involves conducting acoustic beamforming over a series of z -planes using arrays designed for $z = z_0$, and then reconstructing the point source in three-dimensions, comparing its performance to a single array design, as depicted in the schematic diagram in Fig. 1.

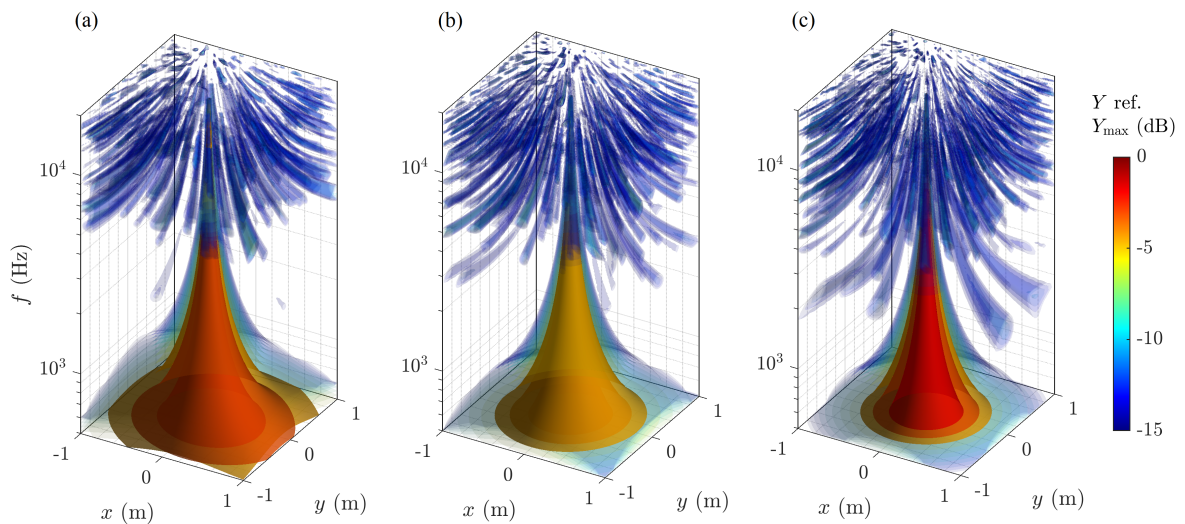


Figure 10: PSF isosurface plots of a source located at $(0, 0, 1)$ m using AARM arrays, derived from the spiral-based initial stencil in Fig. 2(b), designed for 3.5 kHz and (a) $z_0 = 0.5$ m, (b) $z_0 = 1$ m (on-design) and (c) $z_0 = 2$ m. These array patterns are shown in Fig. 8.

4 EXPERIMENTAL VALIDATION

4.1 Set-up

Experiments were conducted using the $M_i = 105$ -channel spiral-based array within the anechoic chamber of the aeroacoustic wind tunnel facility at the University of Twente [19]. A schematic of the set-up is shown in Fig. 11. The set-up included the CAE Systems Bionic M-112 microphone phased array and a custom-build sound source. The sound source featured a Wavecor-TW013WA01 loudspeaker positioned behind a converging duct to create a monopole point source. Further details about this sound source can be found in [20]. To ensure anechoic

conditions, the wind tunnel test section was covered with acoustic (melamine) foam to ensure an anechoic environment. Additionally, the collector of the wind tunnel was covered with 350 mm thick flat absorbers, as depicted schematically in Fig. 11, featuring a perforated metal sheet surface, type G+H SONEX WF350.

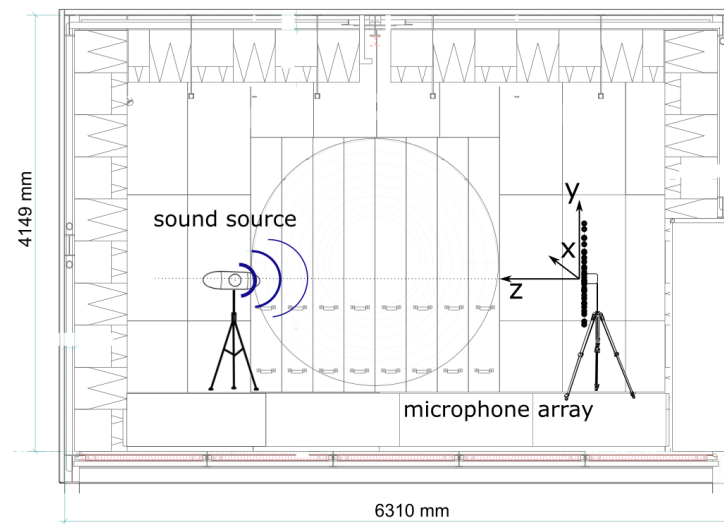


Figure 11: Schematic of the experimental setup.

The loudspeaker of the sound source was excited by white noise. Due to the placement of the loudspeaker behind a converging duct, this configuration resulted in a non-flat frequency response, as depicted in Fig. 12. Positioned at $(x, y) = (0, 0)$ m, the loudspeaker was traversed from $z = 1.0$ m to $z = 3.7$ m in 0.2 m increments. To ensure precise alignment with the microphone phased array, a laser sheet was employed. The microphone signals were sampled at 48 kHz for 20 seconds. In post-processing of the data, the inner-most ring of microphones in the array was omitted from the data analysis, resulting in the use of only 105 microphones.

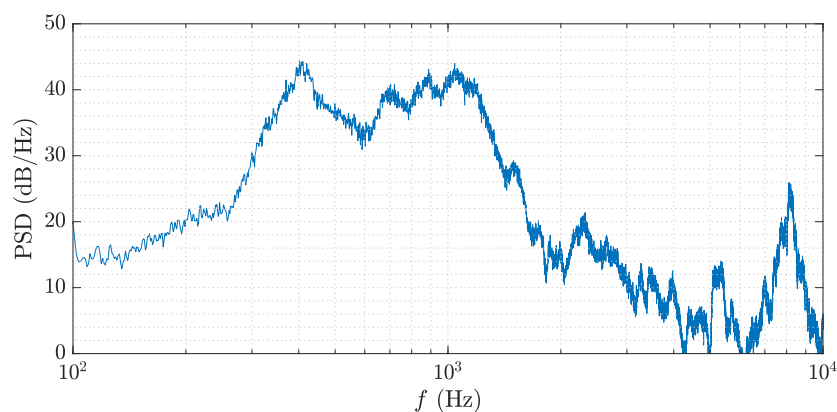


Figure 12: Auto-power spectral density of a microphone near the center of the array. The sound source is emitting white noise and is located at a distance of ($z = 1.0$ m) from the microphone phased array. The reference pressure is $20 \mu\text{Pa}$.

4.2 Results

Figure 13 illustrates the acoustic response of a speaker positioned at $(0,0,z_0 = 1.0)$ m, using the array depicted in Fig. 2(b). These results correspond to the experimental counterpart of Fig. 9(b). Notably, at lower frequencies ($f < 1$ kHz), some asymmetry is observed in the main lobe, potentially attributable to reflections within the testing environment. Around $f \approx 2 - 4$ kHz, the main lobe appears fragmented into smaller lobes, likely due to a diminished signal-to-noise ratio of the speaker, evident from the localized dip in PSD in the corresponding frequency range (Fig. 12). At higher frequencies, the single main lobe structure is restored yet sidelobes become predominant in the source maps. The emergence of prominent sidelobes at higher frequencies, surpassing the numerically-generated PSF equivalent, may stem from minor discrepancies in distance measurements between microphones and the directionality of high-frequency source emitted by a compact speaker.

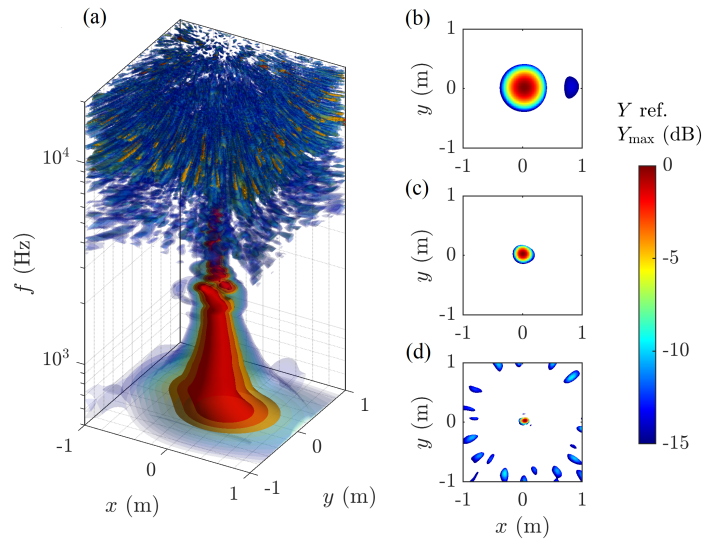


Figure 13: Experimentally-obtained acoustic response of a speaker placed at $(0,0,z_0 = 1)$ m, using the array shown in Fig. 2(b). Image (a) is a PSF isosurface plot and corresponding slices of the PSF are presented at (c) 1 kHz, (d) 2.3 kHz and (e) 5.3 kHz.

The efficacy of the AARM in resolving out-of-plane sound sources is assessed by conducting acoustic beamforming of a speaker source positioned at a known location of z_0 m across a series of planes, z , including z_0 . Initially, the speaker is placed at $(0,0,z_0 = 1.0)$ m, and beamforming is conducted with source planes spanning $z = 1.0$ m to 3.0 m in 0.2 m increments. The initial array (Fig.2(b)) is not tailored for a specific frequency or z_0 -plane. However, it is reduced using the AARM from $M_i = 105$ -channels to $m = 64$ -channels for $f = 5.3$ kHz and $z_0 = 1.0$ m, for comparative purposes with the on-design array configuration. The latter employs AARM arrays designed for each z value across 1.0 m to 3.0 m.

Figure 14 showcases key results from this speaker test, where the red, non-transparent isosurface represents a 3 dB threshold from the peak value. In Fig. 14(a), the 3-D source map reconstruction using $m = 64$ -channels derived from the $M_i = 105$ -channel array is depicted, specifically for $f = 5.3$ kHz and $z_0 = 1.0$ m. At $z_0 = 1.0$ m, the speaker is distinctly located

with some scattered sidelobes within -15 dB, consistent with the PSF isosurface plot and corresponding slices in Fig. 13. However, when $z \neq z_0$, i.e., $z > 1$ m, the main lobe widens, and the sidelobe distribution increases in amplitude and approaches the main lobe. This indicates poor out-of plane resolution despite specific frequency design. By reducing microphones during the AARM process (i.e., terminating the reduction earlier), some improvement in sidelobe amplitude and main lobe strength at $z \neq z_0$ is observed (Figs. 14(b) and 14(d), corresponding to $m = 74$ to 94). At $m = 84$ in Fig. 14(c), the main lobe isosurface becomes disconnected at $z \approx 2.0 - 2.5$ m, indicating signs of some out-of-plane resolution improvement. With more microphones in the AARM array, the detachment length increases (to approx 1.5 m, depicted in Fig. 14(d)).

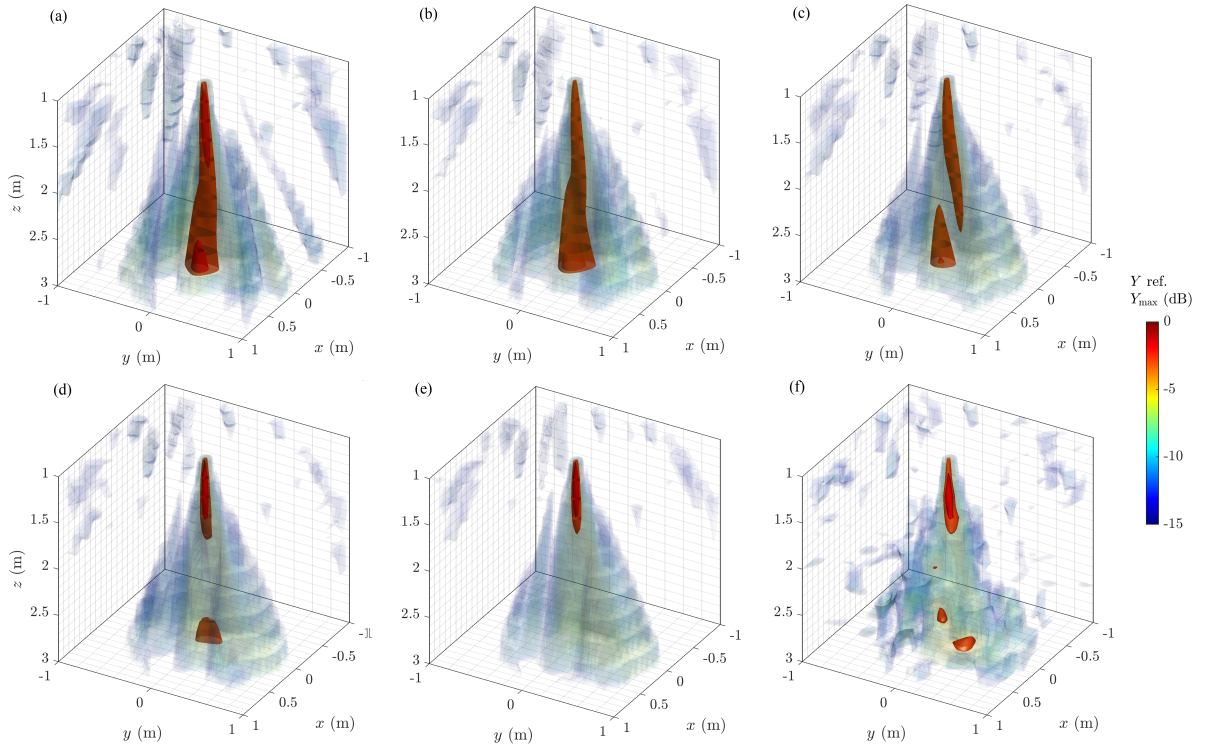


Figure 14: Performance comparison of on- and off-design performance, using experimentally obtained data of the speaker placed at $(0,0,1)$ m. Off-design beamforming conditions, $\Delta z = z - z_0 \geq 0$, using AARM arrays designed for $z_0 = 1$ with (a) $m = 64$, (b) $m = 74$, (c) $m = 84$, (d) $m = 94$, (e) $M_i = 105$ -channel array. Image (f) is the on-design configuration, where AARM arrays are designed for all z -values ($\Delta z = z - z_0 = 0$). Source maps are obtained at $f = 5.3$ kHz.

Using the non-AARM $M_i = 105$ -channel array, only a single main lobe is observed, albeit stretched across $z = 1.0$ m to approximately 1.5 m, as shown in Fig. 14(e). However, applying the AARM on-design configuration with $m = 64$ -channels per array (Fig. 14(f)), yields comparable results to the 94-channel configuration (Fig. 14(d)). The main lobe extends across a similar distance to the 105-channel array, despite additional lobes near $z \approx 2.5 - 3.0$ m. This underscores a promising beginning for the AARM on-design methodology, requiring, in this

instance, 30 fewer microphones than a typical off-design array.

A similar procedure to the one leading to the results in Fig. 14 was also conducted with a speaker placed at $(0,0,z_0 = 1.4)$ m, as depicted in Fig. 15. Across all array configurations, the speaker is accurately localized when $z = z_0$ exhibiting a small main lobe and weak sidelobes. The sidelobe amplitude typically improves with increasing m -values within the off-design arrays. Yet, in this case, the on-design array configuration outperforms all arrays, including the 105-channel array, in terms of out-of-plane resolution and main lobe width, up to a 15 dB limit.

While only two z_0 configurations at a single frequency have been presented in this paper, the results are promising. With future optimization of the on-design methodology and the incorporation of array pairing in conjunction with deconvolution methods such as CLEAN-SC [18], the out-of-plane resolution could be significantly improved using only arrays bound to a single z -plane.

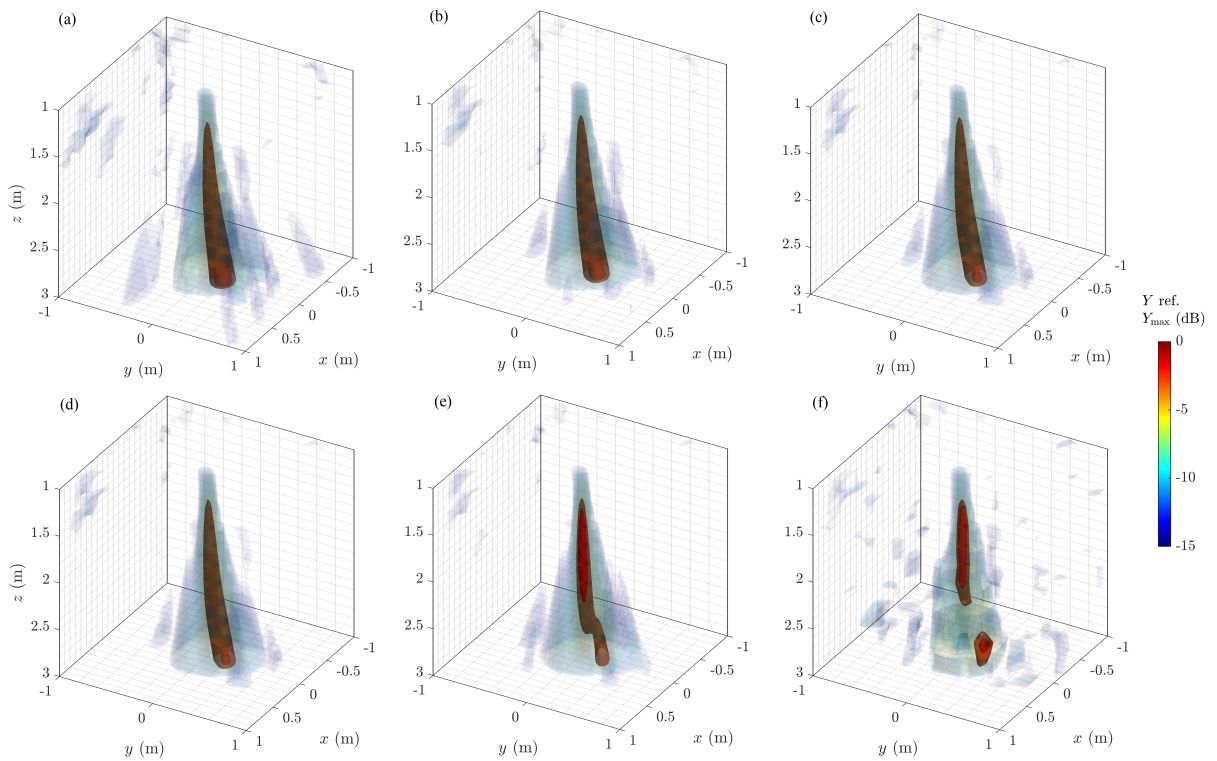


Figure 15: Performance comparison of on- and off-design performance, using experimentally obtained data of the speaker placed at $(0,0,1.4)$ m. Off-design beamforming conditions, $\Delta z = |z - z_0| \geq 0$, using AARM arrays designed for $z_0 = 1.4$ m with (a) $m = 64$, (b) $m = 74$, (c) $m = 84$, (d) $m = 94$, (e) $M_i = 105$ -channel array. Image (f) is the on-design configuration, where AARM arrays are designed for all z -values ($\Delta z = |z - z_0| = 0$). Source maps are obtained at $f = 5.3$ kHz.

5 CONCLUSIONS

A numerical investigation of how the AARM can be used to develop arrays patterns that are suited for specific source planes, $z = z_0$, corresponding to a source located at $(0,0,z_0)$, was conducted. Such array designs are referred to as on-design and off-design conditions. These occur when a source is located at z_0 , either due to lack of prior knowledge or miscalculation, and an array designed for $z \neq z_0$ is used. The off-design condition is the typical condition for an array that is not modified for a specific z -plane. Off-design conditions were tested using an AARM array, against a series of on-design condition AARM arrays. The comparison revealed that the design point AARM arrays can detect a source in 3-D, using a combination of arrays at the same array plane. This is typically not feasible using off-design array patterns without the use of a deconvolution algorithm. The out-of-plane resolution using the on-design framework typically met or surpassed the capability of an off-design array with more microphones.

Clearly, a generalised framework and a wider set of testing parameters are required to better understand how effective the AARM is at improving out-of-plane resolution, such as the development of on- and off-design performance curves. Future work will involve developing such curves to provide guidance in array design selection for a range of operating frequencies, source-plane distances from the array, array aperture and the number of available microphone channels. Nonetheless, the methodology presented in this paper, while preliminary in nature, reveals that the AARM is capable of improving out-of-plane resolution for acoustic beamforming and also help alleviate some uncertainty about the existence of sources in source grid planes other than the source grid plane of interest.

References

- [1] Robert P Dougherty. Spiral-shaped array for broadband imaging. *US Patent, No. 5838284*, 1998.
- [2] James R Underbrink. Aeroacoustic phased array testing in low speed wind tunnels. In *Aeroacoustic Measurements*, pages 98–217. Springer, 2002. doi: 10.1007/978-3-662-05058-3_3.
- [3] Zebb Prime and Con Doolan. A comparison of popular beamforming arrays. In *Proceedings of the Australian Acoustical Society AAS2013 Victor Harbor*, volume 1, page 5, 2013.
- [4] Elias Arcondoulis and Yu Liu. Adaptive array reduction method for acoustic beamforming array designs. *The Journal of the Acoustical Society of America*, 145(2):EL156–EL160, 2019. doi: 10.1121/1.5090191.
- [5] Elias Arcondoulis and Yu Liu. An iterative microphone removal method for acoustic beamforming array design. *Journal of Sound and Vibration*, 442:552–571, 2019. doi: 10.1016/j.jsv.2018.11.005.
- [6] José A Ballesteros, Ennes Sarradj, Marcos D Fernandez, Thomas Geyer, and M^a Jesús Ballesteros. Noise source identification with beamforming in the pass-by of a car. *Applied Acoustics*, 93:106–119, 2015. doi: 10.1016/j.apacoust.2015.01.019.

- [7] Giorgio Baldinelli, Francesco Bianchi, Danilo Costarelli, Francesco D'Alessandro, Flavio Scrucca, Marco Seracini, and Gianluca Vinti. Innovative techniques for the improvement of industrial noise sources identification by beamforming. *Noise Mapping*, 8(1):129–137, 2021. doi: 10.1515/noise-2021-0010.
- [8] Ennes Sarradj. Three-dimensional acoustic source mapping with different beamforming steering vector formulations. *Advances in Acoustics and Vibration*, Volume 2012, 2012. doi: 10.1155/2012/292695.
- [9] Ric Porteous, Zebb Prime, Con J Doolan, Danielle J Moreau, and Vincent Valeau. Three-dimensional beamforming of dipolar aeroacoustic sources. *Journal of Sound and Vibration*, 355:117–134, 2015. doi: 10.1016/j.jsv.2015.06.030.
- [10] Lourenço Tércio Lima Pereira, Roberto Merino-Martínez, Daniele Ragni, David Gómez-Ariza, and Mirjam Snellen. Combining asynchronous microphone array measurements for enhanced acoustic imaging and volumetric source mapping. *Applied Acoustics*, 182:108247, November 2021. doi: 10.1016/j.apacoust.2021.108247.
- [11] Liang Yu, Qixin Guo, Ning Chu, and Rui Wang. Achieving 3d beamforming by non-synchronous microphone array measurements. *Sensors*, 20(24):7308, December 2020. doi: 10.3390/s20247308.
- [12] Thomas Padois, Olivier Robin, and Alain Berry. 3d source localization in a closed wind-tunnel using microphone arrays. In *19th AIAA/CEAS Aeroacoustics Conference*. American Institute of Aeronautics and Astronautics, May 2013. doi: 10.2514/6.2013-2213.
- [13] Robert P Dougherty. Beamforming in acoustic testing. In *Aeroacoustic measurements*, pages 62–97. Springer, 2002. doi: 10.1007/978-3-662-05058-3_2.
- [14] William Humphreys, Jr., Thomas Brooks, William Hunter, Jr., and Kristine Meadows. Design and use of microphone directional arrays for aeroacoustic measurements. *36th AIAA Aerospace Sciences Meeting and Exhibit*, page 471, 1998. doi: 10.2514/6.1998-471.
- [15] Thomas F. Brooks and William M. Humphreys. A deconvolution approach for the mapping of acoustic sources (DAMAS) determined from phased microphone arrays. *Journal of Sound and Vibration*, 294(4):856–879, 2006. doi: 10.1016/j.jsv.2005.12.046.
- [16] Miloš Bjelić, Miodrag Stanojević, Dragana Šumarac Pavlović, and Miomir Mijić. Microphone array geometry optimization for traffic noise analysis. *The Journal of the Acoustical Society of America*, 141(5):3101–3104, 2017. doi: 10.1121/1.4982694.
- [17] Pieter Sijtsma. Clean based on spatial source coherence. *International Journal of Aeroacoustics*, 6(4):357–374, 2007. doi: 10.1260/14754720778335945.
- [18] Elias JG Arcondoulis, Yu Liu, Pengwei Xu, Qing Li, Renke Wei, Yannian Yang, and Nanshu Chen. Experimentally Based CLEAN-SC Array Pairing Method for Distributed Aeroacoustic Sources. *AIAA Journal*, 60(4):2678–2684, 2022. doi: 10.2514/1.J061270.

- [19] Leandro D. de Santana, Martinus P.J. Sanders, and Cornelis H. Venner. The utwente aeroacoustic wind tunnel upgrade. In *2018 AIAA/CEAS Aeroacoustics Conference*, 2018. doi: 10.2514/6.2018-3136. AIAA 2018-3136.
- [20] Martinus P.J. Sanders, Cornelis H. Venner, and Leandro D. de Santana. Slat noise measurements in open-jet, hard-wall and hybrid wind tunnel test sections. *Journal of Sound and Vibration*, 546:117420, 2023. doi: 10.1016/j.jsv.2022.117420.